Earth and Planetary Science Letters 554 (2021) 116664

Contents lists available at ScienceDirect

Earth and Planetary Science Letters

www.elsevier.com/locate/epsl

Partial melting of ultrahigh-pressure eclogite by omphacite-breakdown facilitates exhumation of deeply-subducted crust

Peng Feng [a], Lu Wang [a,*], Michael Brown [a,b], Tim E. Johnson [a,c], Andrew Kylander-Clark [d], Philip M. Piccoli [b]

[a] State Key Laboratory of Geological Processes and Mineral Resources, Centre for Global Tectonics, School of Earth Sciences, China University of Geosciences, Wuhan 430074, China
[b] Laboratory for Crustal Petrology, Department of Geology, University of Maryland, College Park, MD 20742, USA
[c] School of Earth and Planetary Sciences, The Institute for Geoscience Research (TIGeR), Curtin University, GPO Box U1987, Perth WA 6845, Australia
[d] Department of Earth Science, University of California, Santa Barbara, CA 93106, USA

ARTICLE INFO

Article history:
Received 26 May 2020
Received in revised form 17 October 2020
Accepted 29 October 2020
Available online 16 November 2020
Editor: A. Yin

Keywords:
omphacite-breakdown
leucosome
partial melting
ultrahigh-pressure eclogite
exhumation

ABSTRACT

Results from numerical modelling and experimental petrology have led to the hypothesis that partial melting was important in facilitating exhumation of ultrahigh-pressure (UHP) metamorphic rocks from mantle depths. However, the melting reactions responsible are rarely well-documented from natural examples. Here we report microstructural features and compositional data that indicate in situ partial melting dominated by breakdown of omphacite in UHP eclogite from the Sulu belt, China. Diagnostic microstructures include: (i) the presence of in situ leucosome pockets composed of plagioclase, euhedral amphibole, minor K-feldspar and epidote within host zoisite- and phengite-bearing eclogite; (ii) skeletal omphacite within the leucosome pockets that has a lower jadeite content (25–45 mol.%) than rock-forming omphacite (39–54 mol.%); and, (iii) seams of Na-rich plagioclase that extend along grain boundaries separating phengite, quartz and zoisite, and which commonly exhibit low dihedral angles where they terminate at triple grain-boundary junctions. Major oxide proportions of 57 leucosome pockets, calculated using mineral modes and compositions, yield leucodiorite bulk compositions characterized by intermediate SiO_2, high Al_2O_3 and Na_2O, and low K_2O contents. In primitive mantle-normalised trace element diagrams, the leucosome pockets show enrichment in large ion lithophile elements, U, Pb, Zr, Hf and Ti, but depletion in Th and Ta, patterns that are similar to those of rock-forming omphacite. Rather than forming predominantly by breakdown of phengite and/or zoisite, as widely proposed in the literature, the leucosome pockets have petrographic characteristics and major oxide and trace element compositions that are consistent with partial melting dominated by omphacite breakdown. Based on conventional thermobarometry, the eclogite was exhumed from pressure–temperature (P–T) conditions of 3.6–3.1 GPa and 900–840 °C. Partial melting led to the formation of the leucosome pockets, which equilibrated with the rims of surrounding rock-forming garnet and pyroxene during crystallisation. Conventional thermobarometry using rim compositions yields P–T conditions of 1.6–1.2 GPa and 780–690 °C, broadly consistent with calculated phase equilibria and Ti-in-zircon temperatures from zircon overgrowths. Weighted mean ages of ca 217–214 Ma from thin overgrowths on zircon are interpreted to record melt crystallisation. This study provides insight into an overlooked mechanism by which eclogites partially melt during exhumation from UHP conditions, and permits a better understanding of the processes that assist deeply-subducted continental crust to return to shallower depths.

© 2020 Elsevier B.V. All rights reserved.

1. Introduction

Since the discovery of coesite in crustal rocks nearly 40 yrs ago, multiple studies (summarized in Brown and Johnson, 2019) have shown that continental margins can be subducted to depths of more than 100 km, experience metamorphism, and then be exhumed back to lower-to-middle crustal depths where erosion or younger tectonic events facilitate final exhumation to the surface. Although many models have been proposed to explain the exhumation of ultrahigh pressure (UHP) metamorphic rocks (reviewed by Hacker and Gerya, 2013), the role of fluids and/or

* Corresponding author.
E-mail address: wanglu@cug.edu.cn (L. Wang).

https://doi.org/10.1016/j.epsl.2020.116664
0012-821X/© 2020 Elsevier B.V. All rights reserved.

melts is of first-order importance (e.g., Labrousse et al., 2011, 2015; Sizova et al., 2012). Even under the low thermobaric gradients (T/P) that characterise subduction (Brown and Johnson, 2019), UHP rocks should undergo partial melting, most likely during exhumation. Counterintuitively, evidence of melting is more commonly found in eclogites that form a minor component of subducted continental margins in collisional orogens rather than the volumetrically-dominant felsic gneisses. Furthermore, the rock-forming minerals in the felsic gneisses generally do not preserve widespread evidence of UHP metamorphism, probably due to variable metamorphic transformation during subduction and exhumation associated with reaction kinetics and strain heterogeneity in H_2O-deficient rocks (Young and Kylander-Clark, 2015; Garber et al., 2017; Chapman et al., 2019). However, multiple studies of inclusions in zircon from the felsic gneisses have demonstrated that, in many cases, these rocks did reach UHP conditions (Liu and Liou, 2011).

Based on a variety of studies using different techniques, silicate melt produced during high-grade metamorphism is inferred to coalesce along grain boundaries, accumulate in melt pockets and then migrate into larger melt channels to ascend through the crust; at each of these stages melt may partly or wholly crystallise (Brown, 2010; Sawyer et al., 2011; Wang et al., 2014). Constraints on the mechanisms of partial melting of natural eclogite at high pressure (HP) and UHP conditions are limited to a few recent studies focused on leucosome veins or multiphase solid inclusions (MSI) (e.g., Chen et al., 2012, 2014; Gao et al., 2013, 2017; Liebscher et al., 2007; Wang et al., 2014; Wang et al., 2017, 2020; Zhang et al., 2015). Although the compositions of leucosome veins and MSI may provide some constraints on melt composition, in general leucosome compositions reflect modification of primary melts by fractional crystallisation and/or reaction with host rocks (e.g., Sawyer et al., 2011), and whether mineral-hosted MSI in eclogite represent former melt or fluid, or replacement of mineral inclusions is sometimes uncertain (e.g., Gao et al., 2017; Liu et al., 2018; Wang et al., 2016). As a result, melt compositions may be better constrained by millimetric pockets of leucosome that represent the initial stage of melting during which the melt may have remained more-or-less in situ, at least at the scale of a thin section (Brown et al., 1999). Study of leucosome pockets also provides the opportunity to unambiguously determine the melting reaction using a combination of microstructural evidence with mineral modes and compositions.

Partial melting experiments on synthetic or natural basic rock compositions complement studies of natural eclogite from HP and UHP metamorphic belts. Experiments have been performed to elucidate the mechanisms of partial melting and composition of the products under HP and UHP conditions (P = 1.0–7.5 GPa; T = 800–1500 °C) and to constrain the contribution of recycled oceanic crust to ocean island basalts, the source of sodic granites in collisional orogens and the petrogenesis of felsic Archean crust (e.g., Klemme et al., 2002; Laurie and Stevens, 2012; Liu et al., 2009; Pertermann and Hirschmann, 2003; Rapp et al., 2003; Schmidt et al., 2004; Skjerlie and Patiño Douce, 2002). Many natural and experimental studies have concluded that partial melting of H_2O-undersaturated eclogite proceeds by hydrate-breakdown melting, mostly consuming phengite and/or epidote-group minerals at P = 1.5–3.2 GPa and $T \geq$ 800–975 °C (e.g., Gao et al., 2017; Liu et al., 2009; Skjerlie and Patiño Douce, 2002; Song et al., 2014), although some studies have argued for water-saturated partial melting at P = 1.0–3.4 GPa and $T \geq$ 650–770 °C (Labrousse et al., 2011, 2015; Laurie and Stevens, 2012; Mibe et al., 2011) or melting driven by dehydroxylation of nominally anhydrous minerals during the early stages of exhumation at $P \geq$ 3.5 GPa and $T \geq$ 770 °C (Wang et al., 2017, 2020).

Here, we present a detailed petrochemical study of millimetric leucosome pockets inferred to have crystallised in situ within UHP eclogite in the central Sulu belt, China. We combine petrological observations with estimated leucosome compositions, constraints on the P–T conditions and timing of leucosome formation to characterise the earliest stage of partial melting in this UHP eclogite. For the first time, we demonstrate that omphacite breakdown was the primary contributor to melt formation.

Although omphacite is a nominally anhydrous mineral, we note that it typically has water contents from several hundred up to several thousand parts per million (ppm) at UHP conditions (e.g., Katayama et al., 2006; Skogby et al., 2016; Wang et al., 2018, and references therein). Therefore, omphacite is potentially an important source of fluid during exhumation and melting, in addition to any hydrous minerals that may be present. We argue that omphacite-breakdown melting should be common and may have been overlooked in studies lacking detailed microstructural information, with important implications for the mechanisms of melting and exhumation of deeply-subducted crust.

2. Geological background

The Sulu belt, which comprises an HP zone in the south and a UHP zone in the centre and to the north (Fig. 1A), was formed by subduction and collision of the Yangtze craton with the North China craton. UHP eclogites occur as boudinaged remnants of mafic dikes within host felsic orthogneiss, the protoliths of which formed along the northern margin of the Yangtze craton during the Neoproterozoic breakup of the supercontinent Rodinia at ca 800–750 Ma (Liu and Liou, 2011). Based on numerous studies of zircon geochronology linked to the metamorphic evolution via mineral inclusion suites, the regional peak of UHP metamorphism in the Sulu belt occurred between ca 235 and ca 225 Ma with retrograde HP eclogite to amphibolite facies metamorphism from ca 225 to ca 208 Ma (Liu and Liou, 2011).

In the central Sulu belt, outcrops around Taohang are dominated by felsic gneiss containing lenses, blocks and layers of eclogite, all of which are crosscut by granodiorite dykes (Fig. 1B). Coesite inclusions in zircon within the felsic gneiss, together with coesite pseudomorphs in garnet and omphacite within eclogite, demonstrate that both rock types underwent UHP metamorphism (Yao et al., 2000; Ye et al., 2000). Using conventional thermobarometry, Yao et al. (2000) calculated peak pressure of 3.1 GPa (at 800 °C) and peak temperature of 875–860 °C (at 2.8 GPa), and two retrograde stages recorded by successive symplectite mineral intergrowths with P–T conditions of 1.7 GPa/820 °C and 0.9–0.7 GPa/740–700 °C, respectively. By contrast, Nakamura and Hirajima (2010) retrieved peak conditions of 3.4 GPa at 700 °C using a combination of the garnet–omphacite–kyanite–SiO_2 barometer with a new calibration of the garnet–clinopyroxene thermometer. Furthermore, Nakamura and Hirajima (2010) argued for significant cooling to 565 °C (at 1.5 GPa) during exhumation, based on the composition of randomly-analysed rims of garnet and omphacite, and an estimated minimum P of 1.0 GPa, based on the jadeite content of omphacite in symplectites with albite. U–Pb SHRIMP geochronology on zircon from amphibolite at Taohang yielded an age of 228 ± 3 Ma (n = 16) from a domain grown at UHP conditions and an age of 212 ± 2 Ma (n = 7) from a retrograde domain (Liu and Liou, 2011).

More recently, Li et al. (2014) presented results of Ti-in-zircon thermometry from the host migmatitic gneiss at Taohang. For inner mantle domains of zircon around inherited cores, interpreted to record the peak pressure, calculated T is 750–650 °C at P of 3.5–3.0 GPa (from Nakamura and Hirajima, 2010), whereas for outer mantle domains, interpreted as grown from anatectic melt, calculated T is 880–700 °C at an inferred, but unconstrained,

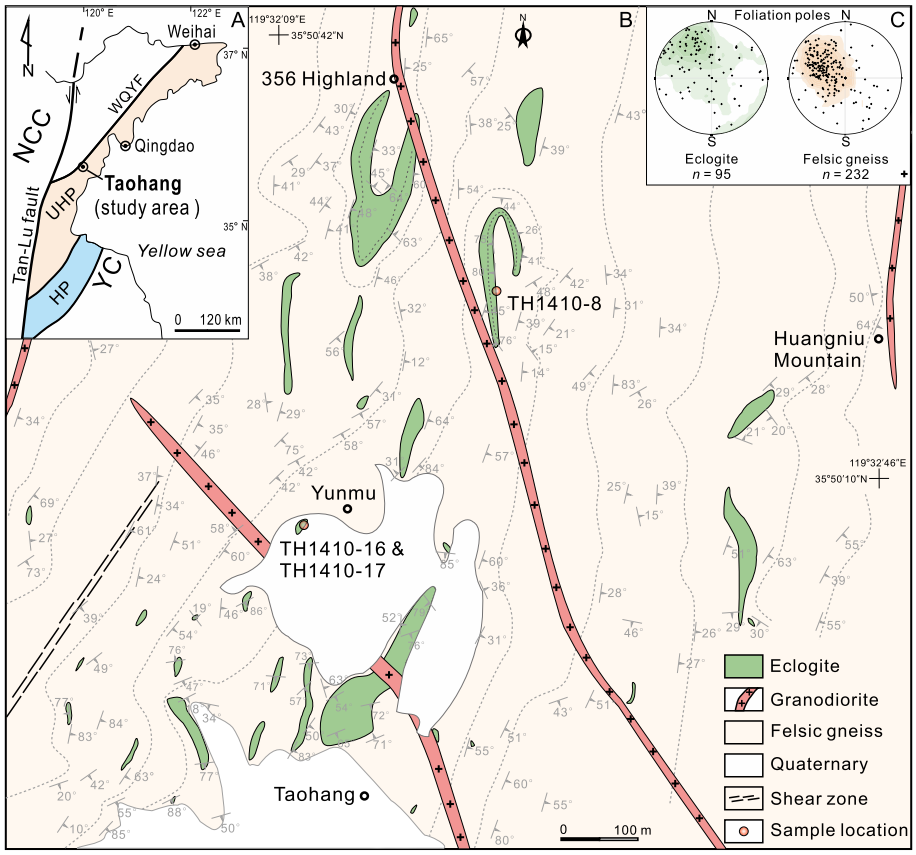

Fig. 1. (A) Simplified geological map of the Sulu belt; YC = Yangtze craton; NCC = North China craton; WQYF = Wulian–Qingdao–Yantai fault; UHP = ultrahigh-pressure metamorphic zone; HP = high-pressure metamorphic zone. (B) Geological map of the study area in Taohang, Sulu belt. (C) Lower-hemisphere equal area projections show the foliation poles of eclogites and felsic gneisses in the study area.

lower pressure. LA–ICP–MS geochronology on these zircon domains yielded ages of 236 ± 5 Ma ($n = 5$) and 223 ± 3 Ma ($n = 8$), respectively (Li et al., 2014).

3. Petrology

3.1. Field relationships and samples

The eclogites at Taohang preserve early rootless isoclinal folds overprinted by tight to open folds (Suo et al., 2009). This study is mostly based on samples of eclogite from a single outcrop (Supplementary Fig. 1A); an additional outcrop was sampled (TH1410-8) for geochronology (sample localities are shown on Fig. 1). Sample TH1410-17 (including fractions TH1410-17-1 and TH1410-17-2, used for geochronology) contains abundant millimetric leucosome pockets that are widely distributed and in places form more continuous irregular veinlets (Fig. 2A). A second sample from this outcrop (TH1410-16), collected from a fold nose, has three petrographically-distinct zones (Fig. 2B, parts A, B and C); part C contains millimetric leucosome pockets that are absent from parts A and B. In this study we focus on those millimetric leucosome pockets that generally do not link to form more continuous irregular veinlets. We infer these leucosomes have crystallised in situ and are likely to have preserved original melt compositions. Mineral abbreviations follow Whitney and Evans (2010).

3.2. Petrography

Eclogite sample TH1410-17 is mainly composed of garnet (37–40 vol.%), omphacite (24–27 vol.%), zoisite (9–12 vol.%), phengite (4–6 vol.%) and quartz (7–10 vol.%), with minor plagioclase (3–5 vol.%), symplectite (3–4 vol.%), kyanite (1 vol.%), amphibole (1 vol.%), rutile (1 vol.%), apatite (1 vol.%) and scarce K-feldspar, biotite and epidote (Fig. 3). Omphacite (Cpx I; Fig. 3A–B), zoisite, phengite, kyanite and rutile occur as inclusions in large (~500–1000 μm) garnet grains. Zoisite contains abundant inclusions of kyanite and omphacite. Coarse-grained (~300–900 μm) omphacite (Cpx II; Fig. 3A–G) rarely contains inclusions of garnet. Plagioclase mostly occurs within leucosome pockets that include highly-irregular skeletal omphacite (Cpx III) and euhedral amphibole (Amp I) (Fig. 3A–H). Although rutile and apatite occur in the eclogite, these accessory minerals are not present in the leucosome pockets. However, 13 of 57 leucosome pockets are in contact with rutile (e.g., Fig. 3I) and three are in contact with apatite (Supplementary Fig. 3Q). In places, rock-forming omphacite is replaced at its margins by a symplectite composed of fine-grained (<50 μm) plagioclase, amphibole (Amp II) and clinopyroxene (Cpx IV), and garnet may be surrounded by a corona of amphibole (Amp III; Supplementary Fig. 2A). In addition, phengite grains may be partly replaced by biotite with or without K-feldspar (Fig. 3C, H, I), and thin reaction rims (~5–20 μm in width) between zoisite and kyanite comprise a mixture of these two minerals (Fig. 3I).

Eclogite sample TH1410-16 is composed of three zones with different mineral assemblages. Part A comprises omphacite (44 vol.%), garnet (37 vol.%), quartz (11 vol.%), amphibole (4 vol.%), zoisite (1 vol.%), plagioclase (1 vol.%), rutile (1 vol.%) and apatite (1 vol.%), with minor kyanite (Supplementary Fig. 2B). Part B contains garnet (73 vol.%), quartz (26 vol.%) and rutile (1 vol.%), with minor K-feldspar and plagioclase (Supplementary Fig. 2C). Part C consists of omphacite (41 vol.%), symplectite (18 vol.%), plagioclase (9 vol.%), garnet (7 vol.%), zoisite (7 vol.%), phengite (5 vol.%), quartz (5 vol.%), amphibole (5 vol.%), kyanite (2 vol.%) and rutile (1 vol.%),

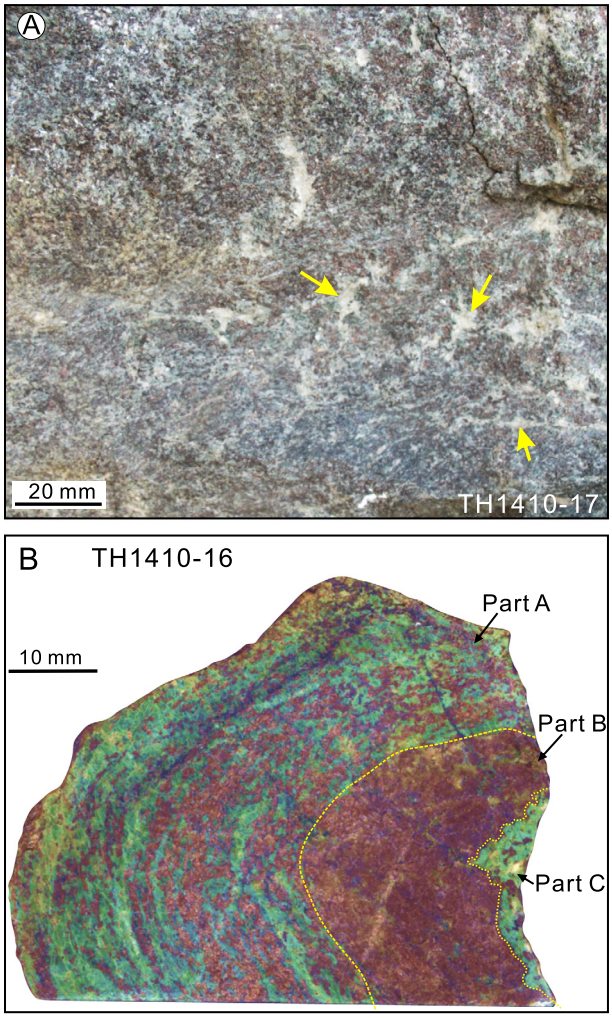

Fig. 2. The leucosome-bearing eclogite at Taohang, Sulu belt. (A) Eclogite outcrop from which sample TH1410-17 was collected. Note the in situ leucosome pockets, as indicated by yellow arrows. (B) Eclogite sample TH1410-16 is composed of three layers with different mineral assemblages, labelled as part A, part B and part C, respectively. Leucosome pockets are only present in part C. (For interpretation of the colours in the figure(s), the reader is referred to the web version of this article.)

with minor K-feldspar and apatite (Supplementary Fig. 2D). In this sample, the symplectite that replaces omphacite at its margins is mainly composed of plagioclase, amphibole and clinopyroxene.

Three lines of evidence in samples TH1410-17 and TH1410-16-part C are consistent with low volume partial melting. First, the presence of leucosome pockets, 200–2000 μm across in thin section, composed of plagioclase, euhedral amphibole, minor K-feldspar and epidote, which occur between coarse-grained garnet, omphacite (Cpx II), phengite and zoisite (Fig. 3A–B; Supplementary Fig. 3A–X; cf. Sawyer, 2001); no evidence of melt infiltration was observed. Second, these leucosome pockets commonly contain highly-irregular skeletal omphacite (Cpx III) intergrown with plagioclase in a texture that we argue is consistent with breakdown of rock-forming omphacite (Cpx II) during incongruent partial melting (Fig. 3A–H). Third, the occurrence of thin seams of Na-rich plagioclase along grain boundaries between phengite, quartz and zoisite that commonly exhibit low dihedral angles where they meet at triple grain-boundary junctions (Fig. 3C–I).

The eclogite samples in which the compositions of multiple leucosome pockets were determined contain 3–7 vol.% leucosome, and in areas around the leucosome pockets 17–36% of mineral grain boundaries are filled with plagioclase pseudomorphs after former melt. Thus, the amount of leucosome suggests that the volume of melt originally in the samples was generally below the melt-connectivity transition (MCT) of Rosenberg and Handy (2005; cf. Sawyer, 2001). At outcrop scale (Supplementary Fig. 1B), larger pockets of leucosome show limited connectivity. Using image analysis, we determined leucosome to comprise 6–8 vol.% of the outcrop shown in Supplementary Fig. 1B, which is around the MCT value, consistent with the limited connectivity observed. These data suggest that it is unlikely that any melt has drained from this outcrop and support the interpretation that the smaller generally isolated leucosome pockets likely represent melt compositions.

4. Analytical results

Details of the analytical methods used are provided in the supplemental material. The major element compositions of minerals were determined at the Centre for Global Tectonics, School of Earth Sciences, China University of Geosciences, Wuhan, using a JEOL JXA-8230 electron probe microanalyser. The trace element composition of minerals was measured using laser ablation–inductively coupled–plasma mass spectrometry (LA–ICP–MS) at the Wuhan Sample Solution Analytical Technology Co., Ltd., Wuhan, China. Whole-rock major and trace element concentrations were determined at the Wuhan Sample Solution Analytical Technology Co. Ltd., Wuhan, China by X-ray fluorescence spectrometer (Rigaku-Primus II) and Agilent 7700e ICP–MS, respectively. U–Pb isotope and trace element compositions in zircon were collected through two different methods. First, we used 'conventional' LA–ICP–MS at the Wuhan Sample Solution Analytical Technology Co. Ltd., and, second, we used 'single shot' laser ablation split-stream (SS–LASS) at the University of California Santa Barbara, as described in detail in the supplementary material.

4.1. Whole-rock major and trace element compositions

The whole-rock major and trace element compositions of parts A, B and C of eclogite sample TH1410-16 and of sample TH1410-17 are listed in Supplementary Table S1. For sample TH1410-16, part A has moderate SiO_2 (49.8 wt.%), $Fe_2O_3^T$ (11.5 wt.%) and Al_2O_3 (15.0 wt.%) concentrations, and high CaO (10.5 wt.%), MgO (7.31 wt.%) and Na_2O (4.29%) contents. It has relatively low total rare earth element contents (ΣREE = 26 ppm) and a moderately fractionated chondrite-normalised REE pattern ($La_N/Yb_N = 3.18$; Supplementary Fig. 4A). In a primitive mantle-normalised multi-element diagram (Supplementary Fig. 4B), part A shows relative enrichment in U, Ba, Sr, Ta and Ti and depletion in Th, Nb and Zr.

Compared to part A, part B contains higher concentrations of SiO_2 (54.9 wt.%), $Fe_2O_3^T$ (16.3 wt.%) and Al_2O_3 (16.1 wt.%), and lower CaO (6.28 wt.%), MgO (4.95 wt.%) and Na_2O (0.06 wt.%) contents. It has lower ΣREE (10.2 ppm) than part A, and is relatively depleted in light REE (LREE) with a flat heavy REE (HREE) pattern ($Gd_N/Lu_N = 0.78$) (Supplementary Fig. 4A). In a primitive mantle-normalised multi-element diagram (Supplementary Fig. 4B), part B shows relative enrichment in Ba, Sr, Ta, Zr, Hf and Ti, but depletion in Th and Nb.

Part C of this sample and sample TH1410-17 contain abundant leucosome pockets and have similar bulk compositions. Compared to part A in sample TH1410-16, they have similar SiO_2 (49.1–50.4 wt.%) and $Fe_2O_3^T$ (11.3–12.3 wt.%) contents, lower MgO (5.28–5.67 wt.%), CaO (9.18–9.65 wt.%) and Na_2O (2.35–3.15 wt.%) concentrations, and higher abundances of Al_2O_3 (16.6–18.5 wt.%) and K_2O (0.54–0.63 wt.%). Both are characterized by significantly higher ΣREE (195 ppm and 99.5 ppm) than part A, with moderate LREE enrichment ($La_N/Sm_N = 2.95$ and 2.82) and shallow HREE patterns ($Gd_N/Lu_N = 1.92$ and 2.01) (Supplementary Fig. 4A). In a primitive mantle-normalised multi-element diagram (Supplementary Fig. 4B), both samples exhibit relative enrichment in large ion

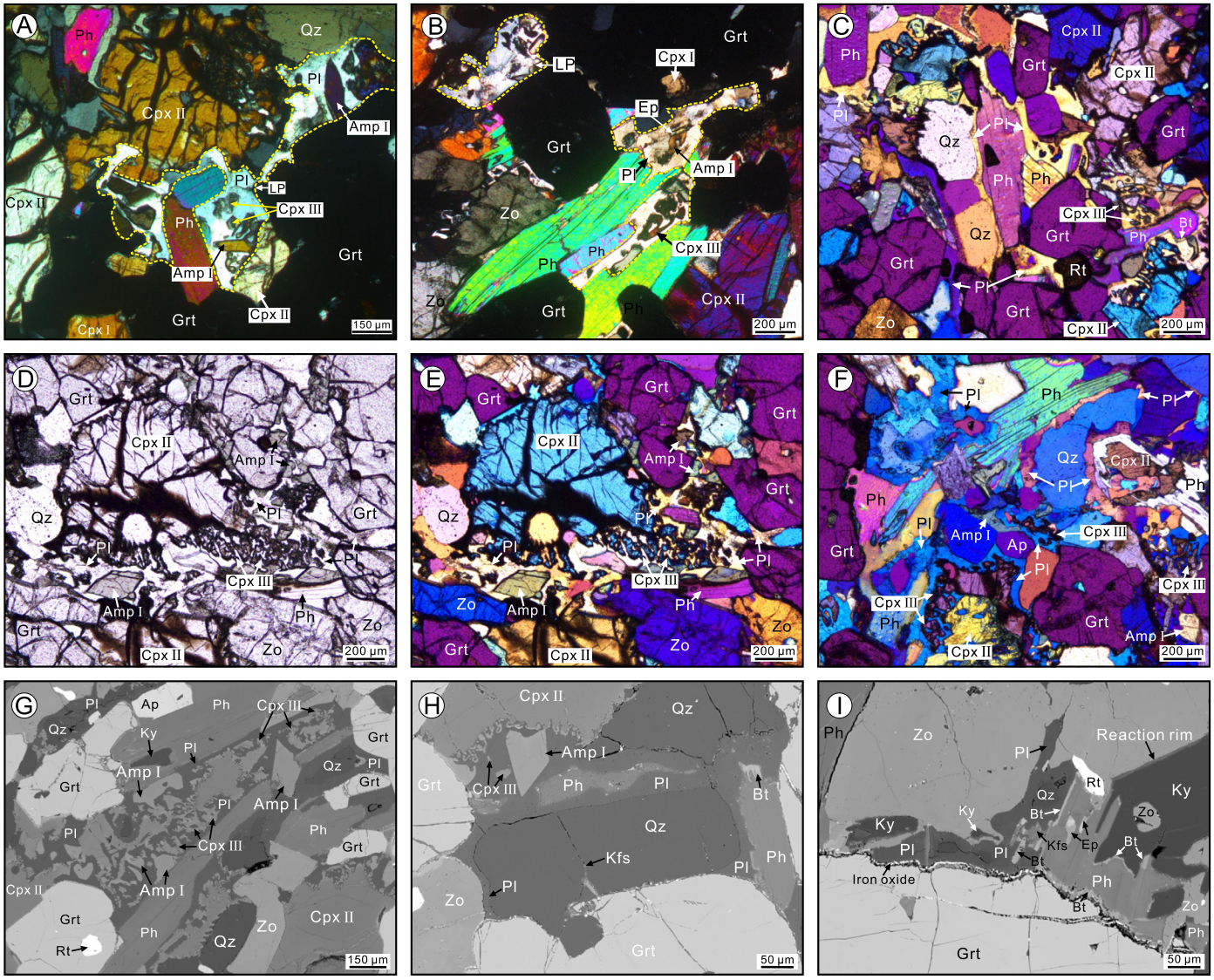

Fig. 3. Representative images to show microstructures indicating partial melting and retrogression in eclogite sample TH1410-17. (A–C, E–F) are in cross-polarized light, (D) is in plane-polarized light, and (G–I) are backscattered electron (BSE) images (note (D) and (E) show the same area). (A–H) show in situ leucosome pockets mainly composed of plagioclase and euhedral Amp I with skeletal omphacite (Cpx III). Note that plagioclase extends along grain boundaries pseudomorphing melt in (C–F), and phengite (C, F) and zoisite (I) grains in contact with leucosome pocket may show irregular (corroded) boundaries. In (A–B), omphacite inclusions (Cpx I) occur in garnet, and in (C, H, I) phengite is partially replaced by Bt ± Kfs. Mineral abbreviations after Whitney and Evans (2010).

lithophile elements (LILE) and depletion in high field strength elements (HFSE) (Supplementary Fig. 4B).

4.2. Mineral compositions

The major element compositions of minerals are listed in Supplementary Table S2. In sample TH1410-17, we also determined the trace element compositions of plagioclase and amphibole grains within the leucosome pockets, coarse-grained garnet, omphacite, phengite and zoisite in contact with leucosome pockets, and accessory rutile and apatite (see Supplementary Table S3).

Garnet

A mapped garnet grain from sample TH1410-17 shows weak zoning in Ca, but broadly constant concentrations of other major cations (Supplementary Fig. 5A–B). Cores are relatively enriched in the grossular component [X_{Grs} = atomic Ca/(Ca + Fe^{2+} + Mg + Mn) = 0.28–0.29] relative to the rims (X_{Grs} = 0.23–0.24; Supplementary Fig. 5B), with $Mg^{\#}$ [= atomic Mg/(Fe^{2+} + Mg)] varying little (0.34–0.37). In part A of sample TH1410-16, garnet grains are essentially unzoned with X_{Grs} of 0.22–0.25 (Supplementary Fig. 5D, E) and $Mg^{\#}$ of 0.36–0.37. In part C, the core of one garnet grain has X_{Grs} of 0.26, increasing to 0.29 in the mantle, then decreasing to 0.25 in parts of the outermost rim; $Mg^{\#}$ varies little from 0.35 to 0.37. The core of another garnet contains a relatively high X_{Grs} of 0.28–0.29, decreasing to 0.24–0.25 in the rim; $Mg^{\#}$ varies from 0.35 to 0.38 from core to rim. Garnet grains contain HREE contents of 22–25 ppm, with Gd_N/Lu_N of 0.28–0.46.

Clinopyroxene

With the exception of four analyses of Cpx IV, clinopyroxene compositions in sample TH1410-17 plot in the omphacite field (Fig. 4A). Different types of clinopyroxene show considerable differences in jadeite concentrations, where X_{Jd} = atomic (Na − Fe^{3+})/[3Na/4 + (Ca + Mg + Fe^{2+})/2 + (Al + Fe^{3+})/4] (Smyth, 1980). The X_{Jd} of omphacite inclusions in garnet (Cpx I) range from 0.39 to 0.53, similar to rock-forming omphacite (Cpx II; X_{Jd} = 0.39–0.54). Cores of Cpx II contain significantly higher X_{Jd} (0.49–0.54) than rims (0.39–0.44) (Supplementary Fig. 5C), whereas finer-grained omphacite (Cpx III) in leucosome pockets

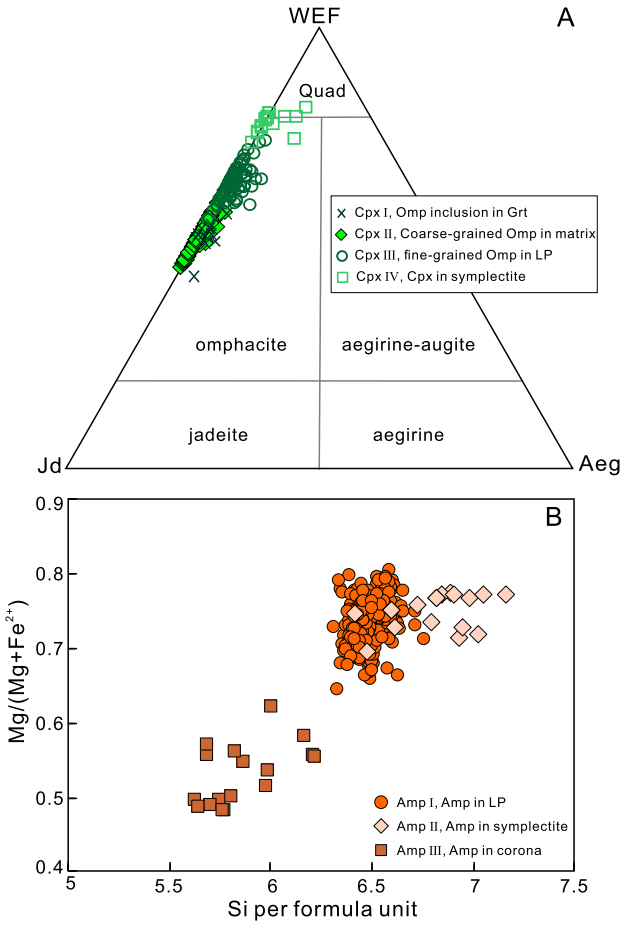

Fig. 4. Compositions of clinopyroxene and amphibole in eclogite sample TH1410-17. (A) In the WEF–Jd–Aeg diagram for sodic clinopyroxene (Morimoto, 1988), almost all compositions are omphacite with a low Aeg component; WEF = wollastonite + enstatite + ferrosilite; Jd = jadeite; Aeg = aegirine; LP = leucosome pocket. (B) Plot of atomic $Mg/(Mg+Fe^{2+})$ versus Si cations per formula unit to show variation in the composition of amphibole.

has much lower X_{Jd} of 0.25–0.45. Lastly, symplectitic clinopyroxene (Cpx IV) contains X_{Jd} of 0.12–0.27. In part A of sample TH1410-16, one omphacite inclusion in garnet has X_{Jd} of 0.45 and rock-forming omphacite has X_{Jd} of 0.42–0.46. In part C, fracture infills within coarse-grained omphacite have X_{Jd} of 0.47–0.52. Finer-grained omphacite in leucosome pockets has significantly lower X_{Jd} (0.33–0.38). Omphacite grains are characterized by enrichment in LILE (e.g., Ba, K, Sr), Pb, Zr, Hf and Ti, depletion in Th, and have ΣREE up to 1.5 ppm (Fig. 5).

Phengite

Phengite is present in sample TH1410-17 and part C of sample TH1410-16, but not in parts A and B. In sample TH1410-17, phengite included in garnet (Ph I) has Si contents of 3.17–3.31 per formula unit (p.f.u.; 11 O basis) and TiO_2 contents of 0.77–1.13 wt.%. Coarse-grained phengite (Ph II) has Si contents ranging from 3.16 to 3.41 p.f.u. and TiO_2 contents varying from 0.70 to 1.17 wt.%. In part C of sample TH1410-16, coarse-grained phengite has Si contents of 3.28–3.37 p.f.u. and TiO_2 contents of 0.48–0.63 wt.%. Phengite is characterized by enrichment in LILE (e.g., Ba, K, Sr), Nb, Pb and Ti, depletion in Ta and contains low REE contents (ΣREE ≪1 ppm) (Fig. 5).

Amphibole

The three varieties of amphibole in sample TH1410-17 are plotted in Fig. 4B. Euhedral amphibole in leucosome pockets (Amp I) has moderate Si contents of 6.31–6.75 p.f.u. (based on 23 O), cationic Na + K of 0.40–0.92 p.f.u. and $Mg^{\#}$ of 0.65–0.81. Symplectitic amphibole (Amp II) has higher Si contents (6.42–7.16 p.f.u.) and a smaller range of both cationic Na + K (0.42–0.69 p.f.u.) and $Mg^{\#}$ (0.70–0.78), whereas amphibole in coronae (Amp III) has lower Si contents (5.62–6.22 p.f.u.), and higher cationic Na + K (0.68–0.86 p.f.u.) and lower $Mg^{\#}$ (0.49–0.62) than Amp II.

In part A of sample TH1410-16, amphibole in fractures within garnet (Amp IV) has a wide range of Si contents (5.69–7.26 p.f.u.), $Mg^{\#}$ (0.59–0.75) and cationic Na + K (0.12–0.73 p.f.u.). By contrast, coarser amphibole replacing omphacite (Amp V) has a narrow range of Si contents (6.45–6.53 p.f.u.) $Mg^{\#}$ (0.68–0.75) and cationic Na + K (0.53–0.61 p.f.u.). In part C of this sample, three analyses of euhedral amphibole in the leucosome pockets (Amp I) have Si contents of 6.35–6.55 p.f.u., $Mg^{\#}$ of 0.72–0.74 and cationic Na + K contents of 0.61–0.74 p.f.u. Amphibole shows enrichment in LILE (e.g., Ba, K, Sr), Pb, Zr, Hf and Ti, depletion in Th and Ta and ΣREE < 4 ppm (Supplementary Fig. 6).

Plagioclase

In sample TH1410-17, plagioclase in the leucosome pockets and thin seams along grain boundaries is oligoclase, with X_{Ab} [= atomic Na/(Na + Ca + K)] values of 0.84–0.90 and 0.84–0.89, respectively. In part A of sample TH1410-16, symplectitic plagioclase replacing omphacite has variable X_{Ab} of 0.64–0.87. In part C, plagioclase in leucosome pocket has X_{Ab} from 0.87 to 0.88. In a primitive mantle-normalised diagram (Supplementary Fig. 6), plagioclase is enriched in LILE (e.g., Ba, K, Sr) and Pb, but depleted in Zr and Ti, and ΣREE < 1 ppm.

Epidote-group minerals

In sample TH1410-17, a zoisite inclusion (Zo I) in garnet has Fe^{3+} content of 0.16 p.f.u. (based on 13 O), whereas a rock-forming zoisite grain (Zo II) has weakly variable Fe^{3+} contents (0.13–0.17 p.f.u.). Fine-grained euhedral epidote in the leucosome pockets has Fe^{3+} contents ranging from 0.36 to 0.53 p.f.u. In part C of sample TH1410-16, a zoisite inclusion within garnet has Fe^{3+} content of 0.17 p.f.u., whereas rock-forming zoisite has Fe^{3+} contents of 0.14–0.15 p.f.u. In a primitive mantle-normalised diagram (Fig. 5), zoisite shows enrichment in Th, U, Pb and Sr, and depletion in HFSE (e.g., Nb, Zr, Hf and Ti). Zoisite is the main repository of REE, with ΣREE = 231–1021 ppm.

Other minerals

Kyanite in all samples is nearly pure Al_2SiO_5. The leucosome pockets in TH1410-17 preserve a small amount of K-feldspar with X_{Or} [= atomic K/(Na + K + Ca)] of 0.93–1.00. Rutile is characterized by enrichment of HFSE (e.g., Nb, Ta, Zr, Hf, Ti), whereas apatite has high contents of P, Sm, Eu and ΣREE (43–82 ppm) (Fig. 5).

4.3. Major and trace element compositions of leucosome pockets

The major and trace element composition of 57 in situ leucosome pockets was determined based on modes and mineral compositions (Supplementary Table S4). In terms of the calculated major oxides (Supplementary Table S5), the leucosome pockets have moderate SiO_2 (55.5–65.7 wt.%), high Na_2O (6.73–9.94 wt.%) and Al_2O_3 (17.3–22.5 wt.%), and low FeO^T (0.07–4.91 wt.%), MgO (0–5.90 wt.%), CaO (2.11–6.37 wt.%), K_2O (0.12–1.33 wt.%) and TiO_2 (0–0.25 wt.%) contents, and classify as leucodiorites. In a primitive mantle-normalised variation diagram, the calculated trace element compositions of 24 leucosome pockets (Supplementary Table S6) show enrichment in LILE (e.g., Ba, K, Sr), U, Pb, Zr, Hf and Ti, and depletion in Th and Ta (Fig. 5). The trace element patterns are generally similar to those of omphacite grains in contact with the leucosome pockets. However, the leucosome pockets are relatively

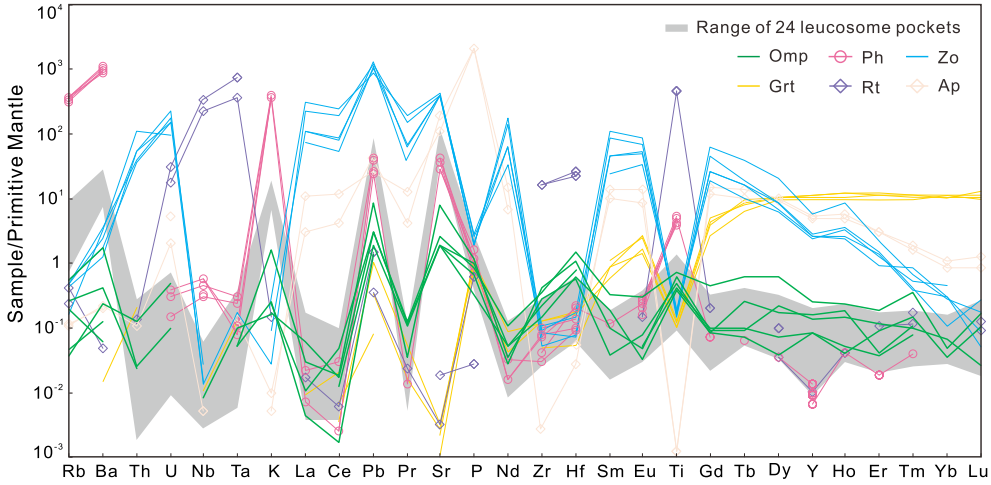

Fig. 5. Primitive mantle-normalised trace element plot for compositions of 24 leucosome pockets. The trace element compositions of omphacite (Omp), phengite (Ph), zoisite (Zo), garnet (Grt), rutile (Rt) and apatite (Ap) in contact with leucosome pockets are plotted for comparison. Values for primitive mantle are from Sun and McDonough (1989).

more enriched in K, with normalised values intermediate between omphacite and phengite, and have higher Pb and Sr concentrations similar to those in phengite (Fig. 5).

4.4. Zircon geochronology and trace element compositions

Zircon grains were separated from two fractions of eclogite sample TH1410-17 (17-1 and 17-2) and from eclogite sample TH1410-8, which all contain leucosome pockets, to determine U–Pb ages and trace element concentrations of both inherited cores and overgrowth rims. Zircon grains are subhedral to anhedral, generally colourless and transparent, and have lengths ranging from 50 to 200 μm with aspect ratios up to 3:1. In cathodoluminescence (CL) images, core domains of zircon generally display oscillatory zoning, whereas rims are homogeneous with a brighter CL response (Fig. 6A, D, G). In general, zircon rims are <10 μm in thickness (Fig. 6A, D, G), which is too thin for conventional LA–ICP–MS analysis. As a result, although the cores were analysed by conventional LA–ICP–MS methods, the rims were analysed using a 'single shot' laser-ablation split-stream (SS–LASS) method (Kylander-Clark et al., 2013). Zircon U–Pb and trace element data are listed in Supplementary Tables S7 and S8, respectively. Uncertainties on all zircon U–Pb ages are quoted at a 2σ level.

Fifteen analyses of oscillatory-zoned zircon cores from sample TH1410-17-1 yield $^{206}Pb/^{238}U$ dates between 765 ± 30 and 295 ± 18 Ma (Fig. 6A), 25 analyses of zircon cores from sample TH1410-17-2 yield $^{206}Pb/^{238}U$ dates from 760 ± 14 to 290 ± 22 Ma (Fig. 6D), and 13 analyses of oscillatory-zoned zircon cores from TH1410-8 yield $^{206}Pb/^{238}U$ dates between 760 ± 23 and 274 ± 13 Ma. Single populations of nine and eight older concordant dates respectively from samples of TH1410-17-1 and TH1410-17-2 yield weighted mean ages of 755 ± 7 Ma (2σ; MSWD = 0.32; Fig. 6A) and 754 ± 6 Ma (2σ; MSWD = 0.30; Fig. 6D), respectively; a weighted mean age could not be determined from sample TH1410-8.

Analyses of CL-bright rims on zircon grains in the same samples yield $^{206}Pb/^{238}U$ dates of 230 ± 12 to 207 ± 15 Ma ($n = 11$), 219 ± 9 to 200 ± 10 Ma ($n = 6$) and 241 ± 9 to 192 ± 16 Ma ($n = 16$), respectively. Weighted mean ages from zircon rims in samples TH1410-17-1, TH1410-17-2 and TH1410-8 are 215 ± 3 Ma (MSWD = 1.5; $n = 10$; Fig. 6B), 214 ± 4 Ma (2σ; MSWD = 1.0; $n = 5$; Fig. 6E) and 217 ± 3 Ma (MSWD = 0.8; $n = 10$; Fig. 6H), respectively. In sample TH1410-8, older dates either contain minor inherited components or represent earlier metamorphic growth, whereas one younger date came from a very thin rim (Fig. 6H).

Oscillatory-zoned zircon cores from these three samples have variable and relatively high Th/U ratios (0.19–2.03), exhibit steep HREE patterns (Gd_N/Lu_N = 0.01–0.06) and have positive Ce [$Ce/Ce^* = 5.06–636.19$, where $Ce/Ce^* = 2 \times Ce_N/(La_N + Pr_N)$] and negative Eu [$Eu/Eu^* = 0.05–0.71$, where $Eu/Eu^* = 2 \times Eu_N/(Sm_N + Gd_N)$] anomalies (Fig. 6C, F, I). By contrast, CL-bright rims have low Th/U ratios (0.01–0.17), flatter HREE patterns (Gd_N/Lu_N = 0.10–0.54) and exhibit positive Ce anomalies ($Ce/Ce^* = 1.10–48.63$) (Fig. 6C, F, I). Analyses included in the mean age calculation show negative Eu anomalies ($Eu/Eu^* = 0.08–0.89$), whereas other analyses exhibit variable Eu anomalies (0.05–1.57) (Fig. 6C, F, I).

Crystallisation temperatures for the zircon rims were calculated using the Ti-in-zircon thermometer of Ferry and Watson (2007), which was calibrated at $P = 1$ GPa and a_{SiO2} and $a_{TiO2} = 1$. For these parameters, temperatures calculated from rims included in the mean age calculations above are shown as box plots in Supplementary Fig. 7. We use the interquartile range of temperatures retrieved from each of the three eclogite samples (Krzywinski and Altman, 2014), which are 625–589 °C, 650–582 °C and 660–589 °C, respectively. However, the thermometer has a pressure dependence of ± 50 °C/GPa. Furthermore, although quartz is present in the leucosome pockets, consistent with $a_{SiO2} = 1$, rutile is not, and even though it does occur at the edge of a minority of leucosome pockets, a_{TiO2} in distributed grain boundary melt may have been unbuffered with $a_{TiO2} < 1$ (Ferry and Watson, 2007). Following Ferry and Watson (2007, p. 435), if a_{TiO2} was as low as 0.5, then calculated temperatures should be raised by 70 °C. Accordingly, the range of Ti-in-zircon temperatures shown in Fig. 7 is for pressures from 1.5 to 0.5 GPa and for a_{TiO2} from 1 (lower bound) to 0.5 (upper bound).

4.5. P–T conditions during exhumation of the UHP eclogite

To constrain the peak P–T conditions of the eclogites we use phengite inclusions in garnet in the barometer of Caddick and Thompson (2008; equation (8)) and core compositions of rock-forming garnet and clinopyroxene (Cpx II) in the thermometer of Ravna (2000) (Supplementary Table S9). The results give P–T conditions of 3.6–3.1 GPa, 900–840 °C (box A in Fig. 7). For the P–T conditions of formation of the leucosome pockets, we combine jadeite-in-clinopyroxene barometry (Carswell and Harley, 1990) with garnet–clinopyroxene thermometry (Ravna, 2000) using the compositions of skeletal omphacite (Cpx III) in the leucosome with rim compositions of rock-forming garnet and clinopyroxene (Cpx

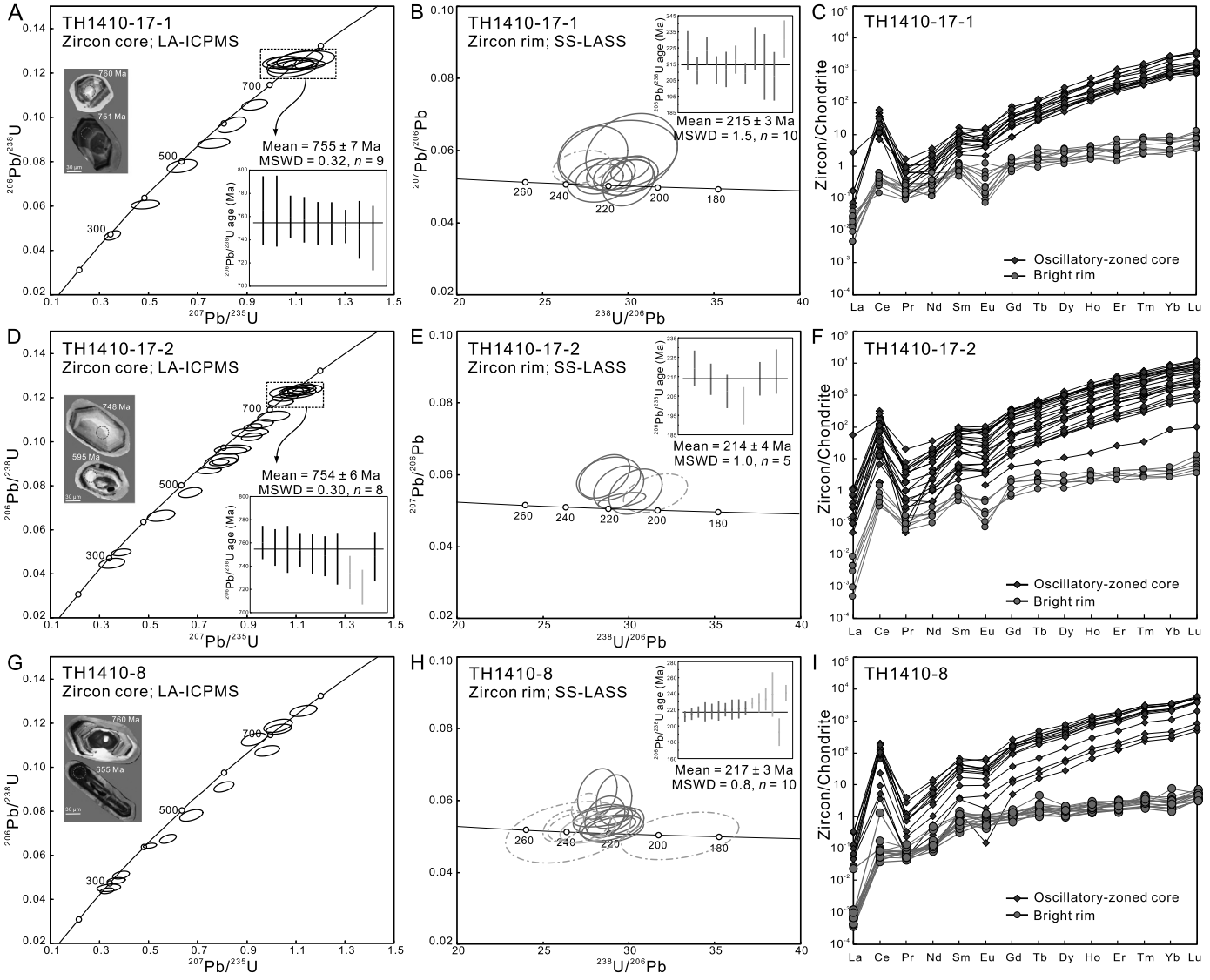

Fig. 6. Geochronology and trace element compositions for zircon from three eclogite samples containing leucosome pockets. Representative cathodoluminescence images of zircon are shown in A, D and G. U–Pb Concordia diagrams for analyses from oscillatory-zoned cores and bright rims are shown respectively in A, D and G, and B, E and H. C, F and I show chondrite-normalised rare earth element (REE) patterns for both zircon cores and rims. In the Concordia diagrams the error ellipses are plotted for 2σ uncertainty; the weighted mean ages are also calculated for 2σ uncertainty. MSWD = mean square of weighted deviates; dates not included in the mean age calculation are shaded in grey. REE values for chondrite are from Sun and McDonough (1989).

II) adjacent to the leucosome. The results constrain conditions to 1.6–1.2 GPa and 780–690 °C (box B in Fig. 7; Supplementary Table S9).

The inferred P–T evolution based on conventional thermobarometry is consistent with calculated phase equilibria for the two leucosome samples (TH1410-16 part C and TH1410-17; Supplementary Fig. 8A, B, respectively). Although activity–composition (a–X) models have not yet been calibrated for clinopyroxene in hydrous melt-bearing systems at HP and UHP conditions, Fig. 7 shows the calculated position of the incoming of hornblende, plagioclase and K-feldspar during exhumation that, within uncertainty, occur at similar P–T conditions for the two samples (Supplementary Fig. 8A, B. Mineral abbreviations follow Holland and Powell 2011.). The calculations, which use THERMOCALC 3.47 (Powell and Holland, 1988) and the a–X models of Green et al. (2016), including the high-pressure omphacite–diopside a–X model, indicate the down-pressure incoming of these minerals occurs at pressures slightly higher than the conditions appropriate to box B in Fig. 7, interpreted to reflect formation of the leucosome pockets. Also shown is the position of the H_2O-undersaturated solidus calculated using an H_2O content corresponding to the loss on ignition (LOI) measured in part C of sample TH1410-16 and in TH1410-17. Although these calculations should be treated with caution, the predicted position of the solidus lies at slightly higher T and P than box B, and may suggest that either the mineral compositions continued to equilibrate after final crystallisation of melt or the measured H_2O content is low. In addition, in Fig. 7 we show the range of Ti-in-zircon temperatures calculated from the composition of zircon rims for a_{TiO2} of 1 and 0.5 as a grey box extending from 1.5 to 0.5 GPa. The ages retrieved from the zircon rims likely record the end of melt crystallisation.

5. Discussion

5.1. Timing of melt crystallisation

The cores of zircon grains within the eclogite are characterized by oscillatory zoning, high Th/U ratios and steep HREE patterns with positive Ce and negative Eu anomalies, consistent with a magmatic origin. The weighted mean ages of these grains (755 ±

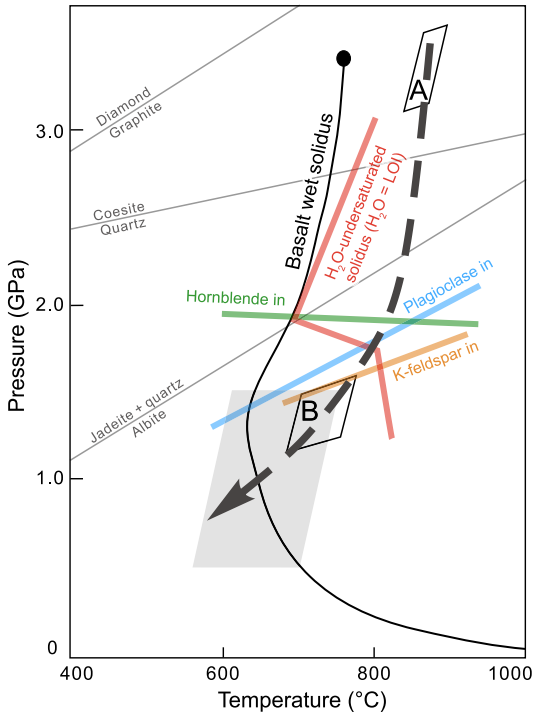

Fig. 7. P–T diagram to show calculated peak P–T conditions (box A) and P–T conditions for crystallisation of the leucosome pockets (box B). The grey box represents the range of Ti-in-zircon temperatures calculated from the Ti concentrations in zircon rims for pressures between 1.5 and 0.5 GPa and for a_{TiO2} from 1 to 0.5, as discussed in the text. The thin black solid line is the wet solidus for basalt (Mibe et al., 2011), which extends to the black dot representing the second critical endpoint for the basalt–H_2O system. The H_2O undersaturated solidus, and the hornblende in, plagioclase in and K-felspar in lines are taken from calculated P–T pseudosections for samples TH1410-16-part C and TH1410-17. A possible P–T path consistent with these constraints is shown by the thick black dashed line.

7 Ma and 754 ± 6 Ma) are similar to protolith ages of metaigneous rocks in the Sulu belt (e.g., Liu and Liou, 2011).

Thin CL-bright zircon rims have relatively low total contents of REE, flat HREE patterns, negative Eu anomalies (Fig. 6C, F, I), low Th/U ratios and relatively low Ti-in-zircon temperatures, which suggest they equilibrated during the late stage of exhumation of the UHP eclogites (Fig. 7). The weighted mean ages of ca 217–214 Ma from these zircon rims fall within the age range of the post-peak retrograde HP eclogite to amphibolite facies metamorphism of ca 225 to 208 Ma for the belt (Liu and Liou, 2011). Combined with P–T conditions during exhumation, we interpret the age range of ca 217–214 Ma to record the final stages of melt crystallisation.

5.2. Comparison with previous studies of melting

Various experimental studies have investigated anatexis of eclogite at high pressures (P = 1.0–7.5 GPa; T = 800–1500 °C). These have mostly used synthetic and/or compositionally-simplified starting compositions lacking K (Kessel et al., 2005) or Fe (Klemme et al., 2002), or anhydrous bimineralic eclogite lacking phengite or zoisite (Pertermann and Hirschmann, 2003), making them unsuitable for comparison with the leucosome pockets at Taohang. Although the experiments of Skjerlie and Patiño Douce (2002) and Liu et al. (2009) at 1.0–3.2 GPa and 1.5–3.0 GPa, respectively, used starting powders of natural zoisite- and phengite-bearing HP or UHP quartz–rutile–kyanite-bearing eclogite with assemblages similar to those of the leucosome-bearing eclogites at Taohang (sample TH1410-17 and part C of sample TH1410-16), in both cases the melts produced are higher in SiO_2 than the leucosome pockets. Lastly, the H_2O-saturated experiments of Laurie and Stevens (2012) at 1.9–3.0 GPa were performed on a natural bimineralic eclogite with quartz and rutile, minor allanite and apatite, and trace phengite and zircon. However, the melt compositions produced were all trondhjemite.

To facilitate comparison of the melt compositions determined in this study with those inferred from a study of quartzofeldspathic MSI thought to have been derived by paragonite-breakdown melting (Chen et al., 2014), and those determined in three experimental studies (detailed below), we use normative An–Ab–Or and 2Al–Si–2(Mg + Fe) triangular diagrams (Fig. 8). It is clear from both diagrams that the leucosome pockets at Taohang have compositions that are distinct from those derived by pargasite-, zoisite- or phengite-breakdown melting, and also from those produced by water-present melting. As discussed below, none of the reactions proposed in these studies is appropriate to the formation of the leucosome pockets at Taohang.

According to Skjerlie and Patiño Douce (2002), at pressures below 1.8 GPa, partial melting of zoisite-bearing eclogite occurs by the reaction Zo + Omp + Ky + Qz ± Grt → melt + Pl + Di ± Opx, and at higher pressures, by the reaction Zo + Omp + Qz → melt + Ky + Di ± Grt. By contrast, Liu et al. (2009) determined that partial melting of phengite-bearing eclogite occurs by the following reactions as pressure increases: at pressures below 2.0 GPa, Omp + Qz + Ky + H_2O → melt + Pl; at pressures of 2.0–2.5 GPa, Omp + Qz + Ph → melt + Pl + Ky; and, at pressures above 2.5 GPa, by the reaction Omp + Qz + Ph → melt + Grt + Jd + Kfs + Ky. However, melting by reactions similar to these does not apply to the leucosome pockets because: (i) the rock-forming zoisite and phengite appear to have largely remained stable; (ii) there is no kyanite, garnet or orthopyroxene observed in the product assemblage; and, (iii) the major and trace element compositions of the leucosome pockets are significantly different to the melt compositions produced in the experiments, which vary with increasing pressure from trondhjemite to granite. In addition, the reactions in Skjerlie and Patiño Douce (2002) require high temperatures (>850 °C at 1.5 GPa to >1025 °C at 2.7 GPa), which are inconsistent with those determined in this study (Fig. 7).

By contrast, Laurie and Stevens (2012) studied water-present melting of quartz-bearing bimineralic eclogite at HP and UHP conditions, in which omphacite and quartz were the principal mineral reactants. Given the P–T results calculated from the leucosome pockets, this study appears to offer a better comparison with the omphacite-breakdown melting implied by our results. However, the melt compositions in the experiments are all trondhjemites and in the partial melting reactions quartz is a major contributor to the melt, as follows (the calculations are anhydrous, and use a 16 oxygen melt molecule, a 12 oxygen Grt molecule and a 6 oxygen Cpx molecule):

$$0.87\ \text{Omp} + 1.00\ \text{Qz} + 0.17\ \text{Grt}_1 + (\text{tr})\ \text{Rt} = 0.14\ \text{Melt} + 0.58\ \text{Cpx} + 0.11\ \text{Grt}_2\ (\text{at } P\text{–}T \text{ of } 2.9\ \text{GPa and } 870\,^{\circ}\text{C});\ \text{and,}$$

$$0.83\ \text{Omp} + 1.00\ \text{Qz} + 0.13\ \text{Grt}_1 + (\text{tr})\ \text{Rt} = 0.13\ \text{Melt} + 0.58\ \text{Cpx} + 0.05\ \text{Grt}_2\ (\text{at } 2.2\ \text{GPa and } 880\,^{\circ}\text{C}).$$

5.3. Mechanism of partial melting at Taohang

For sample TH1410-16, the differences in chemical composition and mineral assemblage between parts A, B, and C are not related to partial melting but are considered to be primary features potentially related to crystal fractionation (e.g., Liu et al., 2008). No evidence for partial melting is preserved in parts A and B of sample TH1410-16. However, in part C of this sample and in sample TH1410-17 small and unconnected in situ leucosome

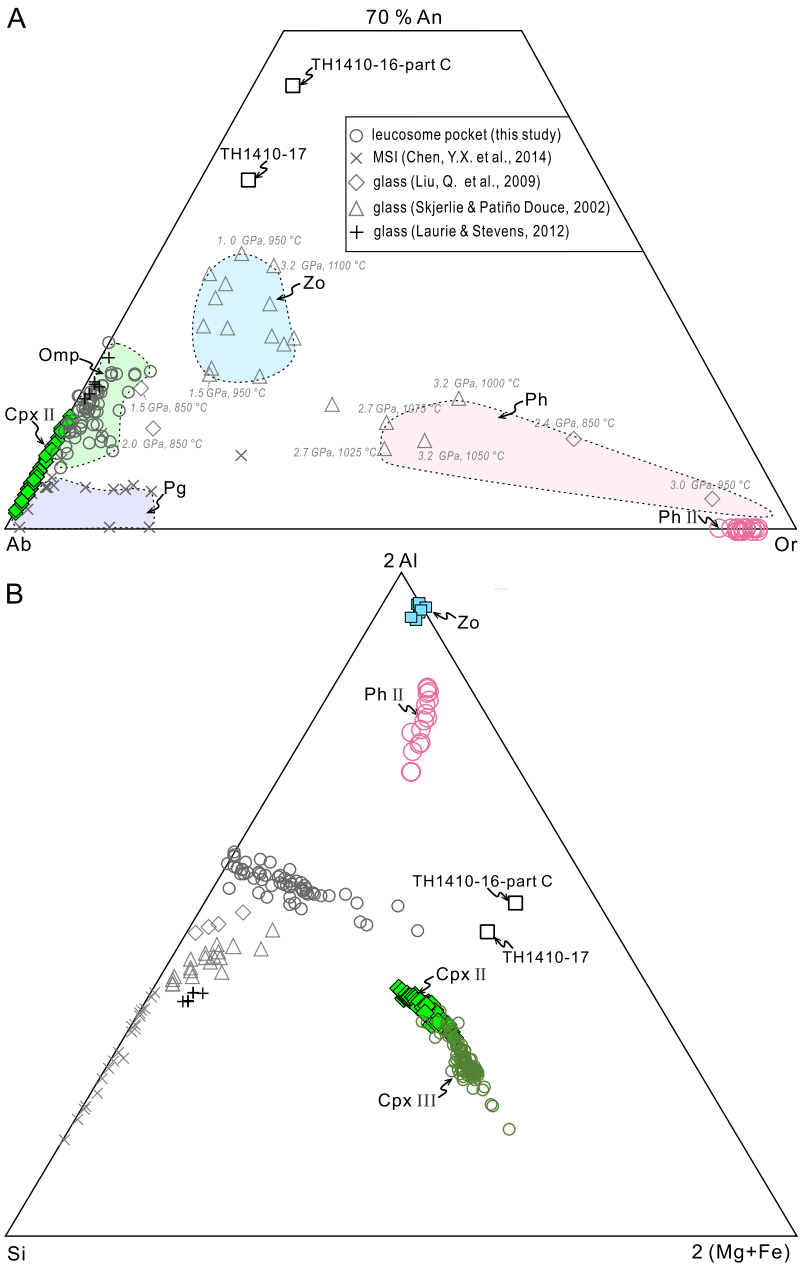

Fig. 8. Major element compositions of 57 leucosome pockets in eclogite sample TH1410-17 from Taohang in terms of CIPW normative feldspar compositions (A) and molar proportions of Al, Si and (Mg + Fe) (B). Also plotted for comparison are the major element compositions of MSI found in UHP zoisite-bearing eclogites from Qinglongshan in the southwestern part of the Sulu orogen (Chen et al., 2014), and glasses from three experimental studies of melting at UHP conditions (Liu et al., 2009; Skjerlie and Patiño Douce, 2002; Laurie and Stevens, 2012) on eclogite with similar mineral assemblages to the peak mineral assemblage in the leucosome-bearing eclogites from Taohang. The different symbols in A and B, and the coloured fields bounded by dashed lines in A, show that partial melting of UHP eclogite by reactions consuming mostly phengite, zoisite, paragonite and omphacite produce distinctly different melt compositions to those represented by the leucosome pockets. The green symbols, open pink circles and blue squares show the measured compositions of clinopyroxene, phengite and zoisite, respectively. The whole-rock compositions of the two eclogite samples are also shown for reference.

pockets record closed system partial melting. Whether rocks melt depends not only on the P–T path but also on bulk composition. The presence of phengite and zoisite in part C, and the higher H_2O content that results, indicate that one or both of these minerals played a minor but key role during partial melting. Although this proposal is supported by the observation that phengite grains in contact with leucosome pockets show some corroded grain boundaries (Fig. 3B, C, F), only minor corrosion of zoisite is observed locally (Fig. 3I) and most zoisite grains are euhedral.

In contrast with the experimental studies discussed above, the leucosome pockets have only moderate SiO_2 with high Al_2O_3 and Na_2O, but low CaO and K_2O contents (Supplementary Table S5). Furthermore, they have trace element compositions that are clearly distinct from adjacent zoisite grains, in particular with respect to U, Th and REE contents (Fig. 5), but relative enrichment in K, Pb and Sr, consistent with minor breakdown of phengite.

In the experiments of Skjerlie and Patiño Douce (2002) at pressures below 3.2 GPa, the product clinopyroxene was less sodic than reactant clinopyroxene, which led these authors to argue that the albite component in the melt was largely supplied by breakdown of the jadeite component of clinopyroxene. Similarly, the melting reactions deduced by Laurie and Stevens (2012) are characterised by the breakdown of the jadeite molecule in the clinopyroxene, together with quartz and water, to form melt in conjunction with

a less sodic clinopyroxene. Although these experiments indicate a key role for clinopyroxene in the partial melting of UHP eclogite, the melt produced in the natural eclogites at Taohang was not as silicic, indicating that the specific melting reaction was different.

At Taohang, skeletal omphacite (Cpx III), which is scattered throughout the leucosome pockets, has a lower jadeite content (X_{Jd} = 0.25–0.45) than coarse-grained omphacite (X_{Jd} = 0.39–0.54) (Fig. 4A), indicating Cpx III represents a peritectic product of the melting reaction. The leucosome has high Na_2O content and similar trace element patterns to nearby rock-forming omphacite (Fig. 5), indicating that partial melting was dominated by omphacite-breakdown. However, the presence of phengite was also necessary for melting to occur, as demonstrated by sample TH1410-16, where layers A and B, which lack phengite, show no evidence of having melted. This interpretation is supported by: (i) the data in Fig. 8B, where the trend of melt compositions away from the 2Al–Si edge is complemented by the trend in omphacite compositions from Cpx II to Cpx III with only a minor contribution required from phengite (Ph II) ± zoisite; and, (ii) the similarity in trace element composition between the omphacite and the leucosome pockets, with the exception of K, Pb and Sr that likely were supplied by a minor phengite component (Fig. 5).

Euhedral amphibole (Amp I) in the leucosome pockets has a different composition than amphibole in the symplectites and coronae (Amp II and Amp III, respectively; Fig. 4B). In addition, tiny euhedral epidote and K-feldspar grains occur in several of the leucosome pockets (Fig. 3B; Supplementary Fig. 6A). Thus, we interpret euhedral amphibole (Amp I), and minor K-feldspar and epidote to have formed during crystallisation of the melts, which also led to partial breakdown of Cpx III and plagioclase.

The leucosome-bearing eclogites contain accessory rutile and apatite. However, the leucosome pockets are depleted in Ta, Sm and Nd (Fig. 5), indicating that these accessory minerals did not contribute significantly to the trace element budget of the leucosome pockets. This inference is consistent with petrographic observations, which show that most leucosome pockets are not in contact with rutile and apatite.

In summary, we argue that partial melting of the Taohang eclogite was dominated by the breakdown of omphacite together with minor phengite. This reaction can be expressed as: Omp (Cpx II) + Ph ± Zo ± Qz → Omp (Cpx III) + melt ± Kfs ± Ep. Based on the average major element compositions of these minerals, and following the method of Laurie and Stevens (2012), we calculate the following melting reaction:

$$1.006\ \text{Omp (Cpx II)} + 0.030\ \text{Ph} + 0.008\ \text{Zo} + 0.100\ \text{Qz} \rightarrow 0.694\ \text{Omp (Cpx III)} + 0.148\ \text{melt}.$$

Subsequently, the melt crystallised to amphibole (Amp I), plagioclase, K-feldspar and epidote.

5.4. Preservation of leucosome pockets at Taohang

In our previous studies in the Sulu belt, isolated melt pockets have been shown to be part of a melt production, migration and transportation system, for example as preserved at General's Hill (Wang et al., 2014). In eclogite bodies, leucosome veinlets at the intergranular scale connect with leucosome veins located along the foliation before merging with leucosome sheets within partially melted country gneisses (Wang et al., 2020). Large composite melt transport systems of this type are thought to critically assist the exhumation of UHP crust (e.g., Labrousse et al., 2011, 2015; Sizova et al., 2012) through melt-enhanced deformation and lubrication of shear zones. Only rare locations preserve in situ leucosome pockets that are isolated and preserve initial melt compositions. At Taohang, outcrops with leucosome pockets occur in fold closures, which represent sites of lower stress than fold limbs, limiting fluid infiltration, melt production and melt migration (cf. Wang et al., 2018). Accordingly, we suggest that future studies in other UHP metamorphic belts target fold closures or low stress area to further investigate the initial stage of melting in exhumed UHP crust.

Our demonstration that the leucosome pockets at Taohang formed by omphacite-breakdown melting has broader implications. If omphacite-breakdown melting is a common phenomenon, at temperatures not much higher than those at Taohang the crust may contain sufficient melt to affect both the density and the strength prior to drainage (Rosenberg and Handy, 2005), which is likely to affect the exhumation mechanism as demonstrated in multiple studies (e.g., Labrousse et al., 2011, 2015; Sizova et al., 2012).

6. Conclusions

This study provides new insight into initial melt compositions and the mechanism of partial melting during exhumation of UHP zoisite- and phengite-bearing eclogites. In the case of the leucosome pockets at Taohang, Sulu belt, our results demonstrate that omphacite-breakdown is the principal contributor to melting with phengite as an essential but minor participant. Omphacite-breakdown melting, which may have been overlooked in the past, is likely to have played a more widespread and critical role than previously thought in facilitating exhumation of subducted continental crust from extreme depths.

CRediT authorship contribution statement

The project was formulated by FP, LW, MB and TJ; all authors were involved in conducting the research, either via acquisition of data or through analysis and interpretation of data. The first draft was written by FP and LW, with input from MB and TJ; all authors were involved in review and editing of the final manuscript. The figures were prepared by FP and TJ, and the tables were prepared by FP.

Declaration of competing interest

The authors declare that they have no known competing financial interests or personal relationships that could have appeared to influence the work reported in this paper.

Acknowledgements

This research was funded by National Natural Science Foundation of China (NSFC Grant 41572182, 42072228), the Ministry of Education of China (BP0719022), the Most Special Fund (MSFGPMR02-3, MSFGPMR30), Open funds GPMR201703, GPMR201704 and GPMR201903 from the State Key Laboratory of Geological Processes and Mineral Resources, China University of Geosciences, and the Fundamental Research Funds for National University (No. CUG-G1323511572). We acknowledge helpful advice from Wenbin Ning.

Appendix A. Supplementary material

Supplementary material related to this article can be found online at https://doi.org/10.1016/j.epsl.2020.116664.

References

Brown, M., 2010. The spatial and temporal patterning of the deep crust and implications for the process of melt extraction. Philos. Trans. R. Soc. A 368, 11–51. https://doi.org/10.1098/rsta.2009.0200.

Brown, M., Johnson, T., 2019. Metamorphism and the evolution of subduction on Earth. Am. Mineral. 104, 1065–1082. https://doi.org/10.2138/am-2019-6956.
Brown, M.A., Brown, M., Carlson, W.D., Denison, C., 1999. Topology of syntectonic melt flow networks in the deep crust: inferences from three-dimensional images of leucosome geometry in migmatites. Am. Mineral. 84, 1793–1818. https://doi.org/10.2138/am-1999-11-1208.
Caddick, M.J., Thompson, A.B., 2008. Quantifying the tectono-metamorphic evolution of pelitic rocks from a wide range of tectonic settings: mineral compositions in equilibrium. Contrib. Mineral. Petrol. 156, 177–195. https://doi.org/10.1007/s00410-008-0280-6.
Carswell, D.A., Harley, S.L., 1990. Eclogites and the eclogite facies: definitions and classification. In: Eclogite Facies Rocks. Blackie, New York, pp. 1–110.
Chapman, T., Clarke, G.L., Piazolo, S., Daczko, N.R., 2019. Inefficient high-temperature metamorphism in orthogneiss. Am. Mineral. 104, 17–30. https://doi.org/10.2138/AM-2019-6503.
Chen, D.L., Liu, L., Sun, Y., Sun, W.D., Zhu, X.H., Liu, X.M., Guo, C.L., 2012. Felsic veins within UHP eclogite at Xitieshan in North Qaidam, NW China: partial melting during exhumation. Lithos 136, 187–200. https://doi.org/10.1016/j.lithos.2011.11.006.
Chen, Y.X., Zheng, Y.F., Gao, X.Y., Hu, Z.C., 2014. Multiphase solid inclusions in zoisite-bearing eclogite: evidence for partial melting of ultrahigh-pressure metamorphic rocks during continental collision. Lithos 200, 1–21. https://doi.org/10.1016/j.lithos.2014.04.004.
Ferry, J.M., Watson, E.B., 2007. New thermodynamic models and revised calibrations for the Ti-in-zircon and Zr-in-rutile thermometers. Contrib. Mineral. Petrol. 154, 429–437. https://doi.org/10.1007/s00410-007-0201-0.
Gao, X.Y., Zheng, Y.F., Chen, Y.X., Hu, Z.C., 2013. Trace element composition of continentally subducted slab-derived melt: insight from multiphase solid inclusions in ultrahigh-pressure eclogite in the Dabie orogen. J. Metamorph. Geol. 31, 453–468. https://doi.org/10.1111/jmg.12029.
Gao, X.Y., Chen, Y.X., Zhang, Q.Q., 2017. Multiphase solid inclusions in ultrahigh-pressure metamorphic rocks: a snapshot of anatectic melts during continental collision. J. Asian Earth Sci. 145, 192–204. https://doi.org/10.1016/j.jseaes.2017.03.036.
Garber, J.M., Hacker, B.R., Kylander-Clark, A.R.C., Stearns, M., Seward, G., 2017. Controls on trace element uptake in metamorphic titanite: implications for petrochronology. J. Petrol. 58, 1031–1058. https://doi.org/10.1093/petrology/egx046.
Green, E.C.R., White, R.W., Diener, J.F.A., Powell, R., Holland, T.J.B., Palin, R.M., 2016. Activity–composition relations for the calculation of partial melting equilibria in metabasic rocks. J. Metamorph. Geol. 34, 845–869. https://doi.org/10.1111/JMG.12211.
Hacker, B.R., Gerya, T.V., 2013. Paradigms, new and old, for ultrahigh-pressure tectonism. Tectonophysics 603, 79–88. https://doi.org/10.1016/j.tecto.2013.05.026.
Holland, T.J.B., Powell, R., 2011. An improved and extended internally consistent thermodynamic dataset for phases of petrological interest, involving a new equation of state for solids. J. Metamorph. Geol. 29 (3), 333–383. https://doi.org/10.1111/J.1525-1314.2010.00923.X.
Katayama, I., Nakashima, S., Yurimoto, H., 2006. Water content in natural eclogite and implication for water transport into the deep upper mantle. Lithos 86 (3–4), 245–259. https://doi.org/10.1016/j.lithos.2005.06.006.
Kessel, R., Ulmer, P., Ulmer, T., Schmidt, M.W., Thompson, A.B., 2005. The water–basalt system at 4 to 6 GPa: phase relations and second critical endpoint in a K-free eclogite at 700 to 1400 °C. Earth Planet. Sci. Lett. 237, 873–892. https://doi.org/10.1016/j.epsl.2005.06.018.
Klemme, S., Blundy, J.D., Wood, B.J., 2002. Experimental constraints on major and trace element partitioning during partial melting of eclogite. Geochim. Cosmochim. Acta 66, 3109–3123. https://doi.org/10.1016/S0016-7037(02)00859-1.
Krzywinski, M., Altman, N., 2014. Visualizing samples with box plots. Nat. Methods 11, 119–120.
Kylander-Clark, A.R.C., Hacker, B.R., Cottle, J.M., 2013. Laser-ablation split-stream ICP petrochronology. Chem. Geol. 345, 99–112. https://doi.org/10.1016/J.CHEMGEO.2013.02.019.
Labrousse, L., Prouteau, G., Ganzhorn, A.C., 2011. Continental exhumation triggered by partial melting at ultrahigh pressure. Geology 39, 1171–1174. https://doi.org/10.1130/g32316.1.
Labrousse, L., Duretz, T., Gerya, T., 2015. H_2O-fluid-saturated melting of subducted continental crust facilitates exhumation of ultrahigh-pressure rocks in continental subduction zones. Earth Planet. Sci. Lett. 428, 151–161. https://doi.org/10.1016/j.epsl.2015.06.016.
Laurie, A., Stevens, G., 2012. Water-present eclogite melting to produce Earth's early felsic crust. Chem. Geol. 314, 83–95. https://doi.org/10.1016/j.chemgeo.2012.05.001.
Li, W.C., Chen, R.X., Zheng, Y.F., Hu, Z.C., 2014. Dehydration and anatexis of UHP metagranite during continental collision in the Sulu orogen. J. Metamorph. Geol. 32, 915–936. https://doi.org/10.1111/jmg.12100.
Liebscher, A., Franz, G., Frei, D., Dulski, P., 2007. High-pressure melting of eclogite and the P–T–X history of tonalitic to trondhjemitic zoisite-pegmatites, Münchberg Massif, Germany. J. Petrol. 48, 1001–1019. https://doi.org/10.1093/petrology/egm008.
Liu, F.L., Liou, J.G., 2011. Zircon as the best mineral for P–T–time history of UHP metamorphism: a review on mineral inclusions and U–Pb SHRIMP ages of zircons from the Dabie–Sulu UHP rocks. J. Asian Earth Sci. 40, 1–39. https://doi.org/10.1016/j.jseaes.2010.08.007.
Liu, P.L., Zhang, J.F., Massonne, H.J., Jin, Z.M., 2018. Polyphase solid-inclusions formed by interactions between infiltrating fluids and precursor minerals enclosed in garnet of UHP rocks from the Dabie Shan, China. Am. Mineral. 103, 1663–1673. https://doi.org/10.2138/am-2018-6395.
Liu, Q., Jin, Z.M., Zhang, J.F., 2009. An experimental study of dehydration melting of phengite-bearing eclogite at 1.5–3.0 GPa. Chin. Sci. Bull. 54, 2090–2100. https://doi.org/10.1007/s11434-009-0140-4.
Liu, Y.S., Zong, K.Q., Kelemen, P.B., Gao, S., 2008. Geochemistry and magmatic history of eclogites and ultramafic rocks from the Chinese continental scientific drill hole: subduction and ultrahigh-pressure metamorphism of lower crustal cumulates. Chem. Geol. 247, 133–153. https://doi.org/10.1016/j.chemgeo.2007.10.016.
Mibe, K., Kawamoto, T., Matsukage, K.N., Fei, Y., Ono, S., 2011. Slab melting versus slab dehydration in subduction-zone magmatism. Proc. Natl. Acad. Sci. 108, 8177–8182. https://doi.org/10.1073/pnas.1010968108.
Morimoto, N., 1988. Nomenclature of pyroxenes. Mineral. Petrol. 39, 55–76. https://doi.org/10.1007/BF01226262.
Nakamura, D., Hirajima, T., 2010. Significant cooling during exhumation of UHP eclogite from the Taohang area in the Sulu region of eastern China and its tectonic significance. Isl. Arc 19, 707–717. https://doi.org/10.1111/j.1440-1738.2010.00739.x.
Pertermann, M., Hirschmann, M.M., 2003. Anhydrous partial melting experiments on MORB-like eclogite: phase relations, phase compositions and mineral–melt partitioning of major elements at 2–3 GPa. J. Petrol. 44, 2173–2201. https://doi.org/10.1093/petrology/egg074.
Powell, R., Holland, T.J.B., 1988. An internally consistent dataset with uncertainties and correlations: 3. Applications to geobarometry, worked examples and a computer program. J. Metamorph. Geol. 6, 173–204. https://doi.org/10.1111/J.1525-1314.1988.TB00415.X.
Rapp, R.P., Shimizu, N., Norman, M.D., 2003. Growth of early continental crust by partial melting of eclogite. Nature 425, 605–609. https://doi.org/10.1038/nature02031.
Ravna, E.K., 2000. The garnet–clinopyroxene Fe^{2+}–Mg geothermometer: an updated calibration. J. Metamorph. Geol. 18, 211–219. https://doi.org/10.1046/j.1525-1314.2000.00247.x.
Rosenberg, C.L., Handy, M.R., 2005. Experimental deformation of partially melted granite revisited: implications for the continental crust. J. Metamorph. Geol. 23, 19–28. https://doi.org/10.1111/J.1525-1314.2005.00555.X.
Sawyer, E.W., 2001. Melt segregation in the continental crust: distribution and movement of melt in anatectic rocks. J. Metamorph. Geol. 18, 291–309. https://doi.org/10.1046/j.0263-4929.2000.00312.x.
Sawyer, E.W., Cesare, B., Brown, M., 2011. When the continental crust melts. Elements 7, 229–234. https://doi.org/10.2113/gselements.7.4.229.
Schmidt, M.W., Vielzeuf, D., Auzanneau, E., 2004. Melting and dissolution of subducting crust at high pressures: the key role of white mica. Earth Planet. Sci. Lett. 228, 65–84. https://doi.org/10.1016/j.epsl.2004.09.020.
Sizova, E., Gerya, T., Brown, M., 2012. Exhumation mechanisms of melt-bearing ultrahigh pressure crustal rocks during collision of spontaneously moving plates. J. Metamorph. Geol. 30, 927–955. https://doi.org/10.1111/j.1525-1314.2012.01004.x.
Skjerlie, K.P., Patiño Douce, A.E., 2002. The fluid-absent partial melting of a zoisite-bearing quartz eclogite from 1.0 to 3.2 GPa: implications for melting in thickened continental crust and for subduction-zone processes. J. Petrol. 43, 291–314. https://doi.org/10.1093/petrology/43.2.291.
Skogby, H., Janák, M., Broska, I., 2016. Water incorporation in omphacite: concentrations and compositional relations in ultrahigh-pressure eclogites from Pohorje, Eastern Alps. Eur. J. Mineral. 38 (3), 631–639. https://doi.org/10.1127/ejm/2016/0028-2533.
Smyth, J.R., 1980. Cation vacancies and the crystal chemistry of breakdown reactions in kimberlitic omphacites. Am. Mineral. 65 (11–12), 1185–1191.
Song, S.G., Niu, Y.L., Su, L., Wei, C.J., Zhang, L.F., 2014. Adakitic (tonalitic-trondhjemitic) magmas resulting from eclogite decompression and dehydration melting during exhumation in response to continental collision. Geochim. Cosmochim. Acta 130, 42–62. https://doi.org/10.1016/j.gca.2014.01.008.
Sun, S.S., McDonough, W.F., 1989. Chemical and Isotopic Systematics of Oceanic Basalts: Implications for Mantle Composition and Processes. Special Publications, vol. 42. Geological Society, London, pp. 313–345.
Suo, S.T., Zhong, Z.Q., Zhou, H.W., You, Z.D., Zhang, L., 2009. Meso- and microstructures of foliated eclogites in Dabie-Sulu UHP belt and implications for the earliest stages of exhumation of UHP metamorphic rocks: an example from Taohang, southeastern Shandong, China. J. Earth Sci. 20, 649–658. https://doi.org/10.1007/s12583-009-0057-5.
Wang, L., Kusky, T.M., Polat, A., Wang, S.J., Jiang, X.F., Zong, K.Q., Wang, J.P., Deng, H., Fu, J.M., 2014. Partial melting of deeply subducted eclogite from the Sulu orogen in China. Nat. Commun. 5 (1), 1–11. https://doi.org/10.1038/ncomms6604.
Wang, L., Wang, S.J., Brown, M., Zhang, J.F., Feng, P., Jin, Z.M., 2018. On the survival of intergranular coesite in UHP eclogite. J. Metamorph. Geol. 36, 173–194. https://doi.org/10.1111/JMG.12288.

Wang, S.J., Wang, L., Brown, M., Feng, P., 2016. Multi-stage barite in partially melted UHP eclogite from the Sulu belt, China. Am. Mineral. 101, 564–579. https://doi.org/10.2138/am-2016-5384.

Wang, S.J., Wang, L., Brown, M., Piccoli, P.M., Johnson, T.E., Feng, P., Deng, H., Kitajima, K., Huang, Y., 2017. Fluid generation and evolution during exhumation of deeply subducted UHP continental crust: petrogenesis of composite granite–quartz veins in the Sulu belt, China. J. Metamorph. Geol. 35, 601–629. https://doi.org/10.1111/jmg.12248.

Wang, S.J., Wang, L., Brown, M., Johnson, T.E., Piccoli, P.M., Feng, P., Wang, Z.L., 2020. Petrogenesis of leucosome sheets in migmatitic UHP eclogites—evolution from silicate-rich supercritical fluid to hydrous melt. Lithos 360–361, 105442. https://doi.org/10.1016/j.lithos.2020.105442.

Whitney, D.L., Evans, B.W., 2010. Abbreviations for names of rock-forming minerals. Am. Mineral. 95, 185–187. https://doi.org/10.2138/am.2010.3371.

Yao, Y.P., Ye, K., Liu, J.B., Cong, B.L., Wang, Q.C., 2000. A transitional eclogite- to high pressure granulite-facies overprint on coesite–eclogite at Taohang in the Sulu ultrahigh-pressure terrane, Eastern China. Lithos 52, 109–120. https://doi.org/10.1016/S0024-4937(99)00087-0.

Ye, K., Yao, Y.P., Katayama, I., Cong, B.L., Wang, Q.C., Maruyama, S., 2000. Large areal extent of ultrahigh-pressure metamorphism in the Sulu ultrahigh-pressure terrane of East China: new implications from coesite and omphacite inclusions in zircon of granitic gneiss. Lithos 52, 157–164. https://doi.org/10.1016/S0024-4937(99)00089-4.

Young, D.J., Kylander-Clark, A.R.C., 2015. Does continental crust transform during eclogite facies metamorphism? J. Metamorph. Geol. 33, 331–357. https://doi.org/10.1111/jmg.12123.

Zhang, G.B., Niu, Y.L., Song, S.G., Zhang, L.F., Tian, Z.L., Christy, A.G., Lei, H., 2015. Trace element behavior and P–T–t evolution during partial melting of exhumed eclogite in the North Qaidam UHPM belt (NW China): implications for adakite genesis. Lithos 226, 65–80. https://doi.org/10.1016/j.lithos.2014.12.009.